SPECIAL
Global Precipitation Measurement (GPM)
COLLECTION

Comparison of TRMM Microwave Imager Rainfall Datasets from NASA and JAXA

YALEI YOU,[a] NAI-YU WANG,[a] TAKUJI KUBOTA,[b] KAZUMASA AONASHI,[c] SHOICHI SHIGE,[d] MISAKO KACHI,[b] CHRISTIAN KUMMEROW,[e] DAVID RANDEL,[e] RALPH FERRARO,[f] SCOTT BRAUN,[g] AND YUKARI TAKAYABU[h]

[a] *Earth System Science Interdisciplinary Center, and Cooperative Institute for Climate and Satellites, University of Maryland, College Park, College Park, Maryland*
[b] *Earth Observation Research Center, Japan Aerospace Exploration Agency, Tsukuba, Japan*
[c] *Meteorological Research Institute, Japan Meteorological Agency, Tsukuba, Japan*
[d] *Graduate School of Science, Kyoto University, Kyoto, Japan*
[e] *Colorado State University, Fort Collins, Colorado*
[f] *NOAA/NESDIS/STAR, College Park, Maryland*
[g] *Laboratory for Atmospheres, NASA Goddard Space Flight Center, Greenbelt, Maryland*
[h] *Atmosphere and Ocean Research Institute, The University of Tokyo, Tokyo, Japan*

(Manuscript received 29 January 2019, in final form 31 December 2019)

ABSTRACT

This study compares three TMI rainfall datasets generated by two versions of NASA's Goddard Profiling algorithm (GPROF2010 and GPROF2017) and JAXA's Global Satellite Mapping of Precipitation algorithm (GSMaP) over land, coast, and ocean. We use TRMM precipitation radar observations as the reference, and also include *CloudSat* cloud profiling radar (CPR) observations as the reference over ocean. First, the dynamic thresholds for rainfall detection used by GSMaP and GPROF2017 have better detection capability, indicating by larger Heidke skill score (HSS) values, compared with GPROF2010 over both land and coast. Over ocean, all three datasets have very similar HSS regardless of including CPR observations. Next, intensity analysis shows that no single dataset performs the best according to all three statistical metrics (correlation, root-mean-square error, and relative bias), except that GSMaP performs the best for stratiform precipitation over coast, and GPROF2017 performs the best for convective precipitation over ocean, based on all three metrics. Finally, an error decomposition analysis shows that the total error and its three components have very different characteristics over several regions among these three datasets. For example, the positive total error in GPROF2010 and GSMaP is primarily caused by the positive hit bias over central Africa, while the false bias in GPROF2017 is largely responsible for this positive total error. For future algorithm development, results from this study imply that a convective–stratiform separation technique may be necessary to reduce the large underestimation for convective rain intensity.

1. Introduction

The Tropical Rainfall Measuring Mission (TRMM) satellite (Simpson et al. 1988; Kummerow et al. 1998), a joint mission between the National Aeronautics and Space Administration (NASA) and the Japan Aerospace Exploration Agency (JAXA) with about 17 years of observations from December 1997 to April 2015 over ~38°S–38°N, greatly improved our knowledge of precipitation vertical structure (Petersen and Rutledge 2001; Liu and Fu 2001; Hirose and Nakamura 2004; You and Liu 2012), extreme precipitation characteristics (Zipser et al. 2006; Hamada et al. 2015), precipitation diurnal cycle (Takayabu 2002; Nesbitt and Zipser 2003), and latent heat release (Tao et al. 1993; Takayabu et al. 2010). TRMM observations have also been used to improve and validate numerical weather prediction models (Pu et al. 2002; Liu et al. 2014; Lien et al. 2016; Figueroa et al. 2016) and were often taken as the reference for the precipitation retrieval algorithm development in the TRMM era (e.g., Kummerow et al. 2001; Wang et al. 2009; Aonashi et al. 2009).

The Precipitation Radar (PR) (Kozu et al. 2001) and the TRMM Microwave Imager (TMI) (Kozu et al. 2001)

Corresponding author: Yalei You, yyou@umd.edu

DOI: 10.1175/JHM-D-19-0022.1

were designed to provide quantitative precipitation estimates. PR measured the surface precipitation rate more directly (Iguchi et al. 2000), while TMI measured the combined effects of the column integrated hydrometeors in the atmosphere (i.e., water path) and the surface emission (e.g., Spencer et al. 1989; Ferraro and Marks 1995; Wang et al. 2009). Therefore, TMI precipitation-rate quality depended more on the precipitation profile characteristics (Petersen and Rutledge 2001; You and Liu 2012; Sohn et al. 2013; Shige and Kummerow 2016) and the surface emission properties (Weng et al. 2001; Prigent et al. 2006; You et al. 2014). Despite TMI's relatively indirect relation with the surface precipitation rate, it had significant value because of its large swath width (880 km) compared to PR (250 km). Other operational microwave radiometers in the TRMM era had even larger swath widths. For most of the TRMM mission lifetime, PR was the only spaceborne radar dedicated to measuring precipitation, while many more microwave radiometers were available (Aonashi et al. 2009; Kummerow et al. 2015), for example, the Advance Microwave Sounding Unit (AMSU), SSM/I, SSMIS, Advanced Microwave Scanning Radiometer (AMSR-E), and Advanced Technology Microwave Sounder (ATMS). Due to the availability and the much wider spatial coverage of these radiometers, the mean revisit time was reduced from several days for PR observations to ~3 h for observations from these passive microwave radiometers (Hou et al. 2014).

Precipitation rate estimates from these microwave radiometers served as the cornerstone for the widely used level-3 gridded precipitation dataset known as the TRMM Multisatellite Precipitation Analysis (TMPA) (Huffman et al. 2007). Previous studies have evaluated and documented the essential features of level-3 merged precipitation products (Joyce et al. 2004; Kubota et al. 2009; Tian et al. 2010; Chen et al. 2013a,b; Yong et al. 2015). Maggioni et al. (2016) reviewed these studies and showed that merged satellite products are generally more accurate over flat terrain, over densely vegetated regions, and in the warm season. We demonstrate later that these features are actually inherited from the level-2 (swath) microwave radiometer precipitation datasets.

NASA and JAXA have independently developed their own TMI rainfall datasets using different algorithms, that is, the Goddard Profiling algorithm (GPROF) of NASA (Wang et al. 2009; Kummerow et al. 2011, 2015), and Global Satellite Mapping of Precipitation project (GSMaP) algorithm of JAXA (Aonashi et al. 2009). This study uses two versions of the TMI rainfall dataset (versions 7 and 8, hereafter V7 and V8) generated by GPROF2010 and GPROF2017 (more details in the following section), and the latest version (version 7, hereafter V7) GSMaP TMI rainfall dataset. Two GPROF TMI datasets are used because, at the time of writing, 1) the TMI rainfall dataset generated by GPROF2010 (V7) was used in the level-3 merged satellite precipitation products (Huffman et al. 2007), and 2) compared with GPROF2010, GPROF2017 (V8, applied to TMI in early 2018) made several major changes and its product characteristics were largely unknown. We use the algorithm names to represent these three rainfall datasets, unless otherwise stated. That is, GPROF2010 for NASA's V7 dataset, GPROF2017 for NASA's V8 dataset, and GSMaP for JAXA's V7 dataset.

Previous studies have compared the older versions of TMI rainfall datasets from NASA and JAXA. For example, Kubota et al. (2007) compared version 6 of the NASA and JAXA TMI rainfall datasets and concluded that the JAXA dataset agreed better with PR observations, especially over land. By decomposing the error into detection and retrieval components, Seto et al. (2009) found that the JAXA dataset (V4.7) has smaller detection and retrieval errors over land compared with the NASA dataset (V6). Taniguchi et al. (2013) noticed the severe underestimation for Typhoon Morakot rainfall rate over Taiwan in both GSMaP and GPROF products (V6) due to terrain effects. Therefore, they proposed an orographic rainfall rate correction scheme and implemented it in the JAXA V7 dataset.

The objective of this study is to compare the performance of rainfall detection and intensity estimates among these three rainfall datasets. This study also attempts to explain where and why these datasets differ and agree. Finally, we hope that this study can benefit the ongoing NASA and JAXA Global Precipitation Measurement (GPM) dataset development, which is built upon the TRMM heritage, by understanding the weaknesses and strengths of each dataset. Throughout this work, we primarily use the PR observations as the reference, though we also include *CloudSat* Cloud Profiling Radar (CPR) observations as part of the reference over ocean since all three TMI rainfall datasets consider rainfall intensity beyond the PR detection capability (Kummerow et al. 2011; Kida et al. 2010).

2. GPROF2010, GPROF2017, and GSMaP algorithms

Previous studies have documented these algorithms in detail, including Wang et al. (2009), Gopalan et al. (2010), and Kummerow et al. (2011, 2015) for GPROF2010 and GPROF2017, and Kubota et al. (2007), and Aonashi et al.

(2009) for GSMaP. This section only briefly summarizes these algorithms to point out their major differences.

a. GPROF2010 and GPROF2017

GPROF2010 uses different retrieval approaches over land and ocean. Over land, it first identifies pixels with the brightness temperature (TB) differences between V21 and V85 (V = vertically polarized) greater than 8 K as precipitating pixels (McCollum and Ferraro 2003; Wang et al. 2009). Additional screening over dessert and snow-covered regions is also applied (Ferraro et al. 1994, 1998; McCollum and Ferraro 2005; Wang et al. 2009). Then, precipitation rates are estimated by regression methods only for the flagged precipitating pixels. Specifically, two regression curves derived from the PR and TMI observations convert TB to precipitation rate for convective and stratiform precipitation systems separately. The final precipitation rate is a weighted average of the convective and stratiform precipitation rates (Wang et al. 2009; Gopalan et al. 2010). The convective/stratiform information for each pixel is derived from three types of TB features, including TB polarization at 10, 37, and 85 GHz, TB spatial variation at 85 GHz, and TB minima at 85 GHz (Gopalan et al. 2010). Over ocean, the precipitation rate is a weighted average of the precipitation rates in the predefined TB–precipitation databases under different sea surface temperature (SST) and total precipitable water (TPW) regimes through a Bayesian retrieval algorithm (Kummerow et al. 2011). Each pixel is associated with a nonzero precipitation rate although a large majority of them are very close to zero (less than 0.01 mm h^{-1}). The probability of precipitation (POP) can be used to determine the precipitating status of each pixel for different applications. GPROF2010 applies the land algorithm over coastal regions, leading to poorer detection and intensity retrieval results (see section 5) along coasts.

The most significant differences between GPROF2010 and GPROF2017 are 1) the Bayesian approach is applied to all surface types, 2) the predefined TB precipitation database is stratified by surface temperature, TPW, and 14 self-similar surface types, and 3) a rain–no-rain detection procedure is explicitly applied in GPROF2017 using different POP values.

b. GSMaP

Similar to GPROF2017, GSMaP employs a uniform framework over all surface types (land, ocean, and coast) for precipitation detection and intensity estimation (Kubota et al. 2007; Aonashi et al. 2009). The GSMaP rainfall detection method over land also uses the TB difference between V21 and V85, but the threshold value is determined at each 1° grid box for each month (Seto et al. 2005, 2008). Yamamoto et al. (2017) improved the detection performance over the Tibetan Plateau using an updated surface emissivity database. Over ocean, the scattering signature from 85 GHz and emission signature from 37 GHz are used to detect deep and shallow rain systems, respectively (Kida et al. 2009). Shallow rainfall detection is further improved by including the wind speed from reanalysis dataset and by assuming more realistic liquid water path values in the radiative transfer computation.

For precipitation intensity estimation, a lookup table (LUT) links TB and precipitation rate in each 5° grid box. A major difference between GPROF and GSMaP is that GSMaP utilizes 10 general types of precipitation profiles (six over land and four over ocean and coast) and one special type of precipitation profile (orographic rain) in the radiative transfer simulation process, while GPROF uses the instantaneous precipitation profiles. Orographic rain is determined by the global objective analysis data from the methods of Shige et al. (2013, 2014), Taniguchi et al. (2013), and Yamamoto and Shige (2015).

c. Consistency in surface types

The surface type (land, ocean, and coast) definition among these three algorithms is different, and a pixel may be associated with different surface types in these three datasets, which is especially true over coastal regions. For example, GPROF2017 has the largest number of coastal pixels, while GSMaP has the smallest number of coastal pixels due to the dynamic surface-type classification developed by Mega and Shige (2016). To avoid this definition inconsistency, this study only uses pixels when all three datasets agree with each other regarding the surface type.

3. Datasets

This study primarily uses five datasets, including two datasets from TRMM PR (2A25 and 2A23, V7), along with the GPROF2010, GPROF2017, and GSMaP rainfall datasets. We use the full record of PR and TMI observations from December 1997 to April 2015. Since PR had intermittent observations from October 2014 to April 2015, this study only uses data when both PR and TMI observations are available. The increase in TRMM's altitude in 2001 shows little influence on our analysis. Following variables from PR products are selected: near surface rain rate, ice/liquid water path from 2A25, and storm-top height and rain type (i.e., convective and stratiform) from 2A23. The rain rate and surface type are obtained from each of the TMI rainfall datasets.

The latest CPR rain rate product over ocean (version 5, 2C-RAIN-PROFILE) from April 2006 to October

TABLE 1. Dataset names, their versions, and variables used in this study. The algorithm names (GPROF2010, GPROF2017, and GSMaP) are added in the parentheses after each TMI rainfall dataset. This study uses these three algorithm names to represent their corresponding TMI rainfall datasets in the discussion, unless otherwise stated.

Satellite name	Sensor name	Product name	Version	Parameters
TRMM	PR	2A25	Version 7	Rain rate, water path
	PR	2A23	Version 7	Storm top height, convective/stratiform
	TMI	2A12 (GPROF2010)	Version 7	Rain rate, surface type
	TMI	2AGPROFTMI (GPROF2017)	Version 8	Rain rate, surface type
	TMI	rain-TMI (GSMaP)	Version 7	Rain rate, surface type
CloudSat	CPR	2C-RAIN-PROFILE	Version 5	Rain rate, rain quality flag

2016 is used. *CloudSat* experienced a battery anomaly in April 2011 and has been in day-only operation-mode since November 2011. Our analysis shows some small differences by including the day-only operation-mode data, but the major conclusions hold. A key reason for including the day-only observations is to increase the collocated sample size between PR and CPR. Datasets, their versions, and variables used in this study are summarized in Table 1.

4. Methodology

a. Collocation scheme

GSMaP produces rain rates at 0.1° resolution (roughly 10 km in the TRMM region), while GPROF2010 and GPROF2017 produce rain rates at 21 and 19 GHz footprint sizes, corresponding to ~18.9 km × 31.1 km and ~20.9 km × 34.6 km, respectively. This study takes the GPROF2017 resolution (19-GHz footprint size) as the nominal resolution. For GSMaP, the weighted-average rain rate according to the distance from the closest eight pixels ($20.9 \times 34.6/10/10 \approx 8$) is taken as the rain rate at this resolution. Since GPROF2010 and GPROF2017 have very similar resolutions, GPROF2010's original resolution remains unchanged.

Because TMI has a much wider swath than PR, we use the central 10 scan-line observations from TMI to ensure full coverage over the PR swath. PR has a horizontal resolution of ~5 km at nadir. The weighted-average rain rate according to the distance from the closest 29 pixels ($20.9 \times 34.6/5/5 \approx 29$) is taken as the PR's rain rate at the nominal resolution. Next, a raining pixel is judged as convective when at least half of the raining pixels out of these 29 PR pixels are convective. Similarly, a raining pixel is judged as stratiform when at least half of the raining pixels out of these 29 PR pixels are stratiform.

For the nadir-looking CPR, the horizontal pixel resolution is 1.4 km × 1.8 km. We first average the rain rates from 20 CPR pixels ($34.6/1.8 \approx 20$) to roughly match the GPROF2017 resolution. When CPR and TMI are less than 5 km and 5 min away from each other, we consider them coincident. These threshold values (5 km and 5 min) are chosen by considering the trade-off between the matchup sample size and the accuracy. While choosing different threshold values affects the quantitative results, the major conclusions hold.

By using these criteria, there are 6257 collocated pixels between CPR and GPROF2017. CPR has severe attenuation issues for heavy rainfall (e.g., Haynes et al. 2009; Wang et al. 2018), so this study only uses the CPR rain rates with "moderate confidence" and "high confidence" as indicated by the rain quality flag. Furthermore, this study only uses the CPR rain rate when the rain rate from PR is zero. Specifically, a pixel judged as a nonraining pixel by PR is determined as a raining pixel when CPR indicates that this pixel is raining. By doing so, there are more light rainfall events, which makes it more difficult to detect for TMI. Indeed, results later show that the detection performance becomes worse when the CPR rain rates are included. This result is understandable because light rainfall events are more difficult to detect in nature.

b. Rainfall detection

To assess the rainfall detection performance, four numbers in a 2 × 2 contingency table (hit, miss, false alarm, and correct negative) are computed (Wilks 2011). A hit is defined as both the reference (e.g., PR) and the TMI retrieval (e.g., GPROF2010) detecting rainfall. A false alarm is when the TMI retrieval detects rainfall while the reference does not, while a miss is when the reference detects rainfall but the TMI retrieval does not. A correct negative is when both the reference and the TMI retrieval detect no rainfall. This study uses 0.2 mm h^{-1} as the rain–no-rain threshold value. We also calculate the detection statistics using 0.1 and 0.5 mm h^{-1} as threshold values. A smaller (larger) threshold value results in worse (better) detection performance [larger Heike skill score (HSS) value] for all three TMI rainfall products. However, the rank of these three products does not change with different threshold values. For this reason, we only present the results with 0.2 mm h^{-1} as the threshold value.

For clarity and to distinguish these four numbers from the later total error component analysis, we refer to these numbers as the: (i) hit number, (ii) false alarm number, (iii) miss number, and (iv) correct negative number. Similar to Tan et al. (2016), these four numbers are shown as percentage values of the total sample because their absolute values are extremely large from ~17 years of observations. That is, each number is divided by the total sample size N ($N = a + b + c + d$). This study further computes the accuracy metrics derived from these four numbers, including probability of detection (POD), false alarm rate (FAR), and HSS. These metrics are calculated as follows:

$$\mathrm{POD} = \frac{a}{a+c},$$

$$\mathrm{FAR} = \frac{b}{b+d}, \quad \text{and}$$

$$\mathrm{HSS} = \frac{2(ad-bc)}{(a+c)(c+d)+(a+b)(b+d)}. \tag{1}$$

The POD (FAR) values vary from 0 to 1 with a larger POD (smaller FAR) indicating better detection performance. A large POD value is often associated with a large FAR value, which makes it difficult to directly compare detection performance using POD or FAR. For this reason, this study uses the HSS value to judge the overall detection performance with a larger HSS value indicating a better overall performance.

c. Rainfall intensity comparison

For the observations in the hit category, three statistical metrics are computed, including correlation coefficient (CC), root-mean-square error (RMSE), and relative bias (RB). Let $\mathrm{R1}_i$ and $\mathrm{R2}_i$ represent rain rates from PR and TMI ($i = 1, \ldots, a$) in the hit category. Then,

$$\mathrm{CC} = \frac{\sum_{i=1}^{i=a}(\mathrm{R1}_i - \overline{\mathrm{R1}})(\mathrm{R2}_i - \overline{\mathrm{R2}})}{\sqrt{\sum_{i=1}^{i=a}(\mathrm{R1}_i - \overline{\mathrm{R1}}) \times \sum_{i=1}^{i=a}(\mathrm{R2}_i - \overline{\mathrm{R2}})}},$$

$$\mathrm{RMSE} = \frac{1}{a}\sum_{i=1}^{i=a}(\mathrm{R2}_i - \mathrm{R1}_i)^2, \quad \text{and}$$

$$\mathrm{RB} = \frac{\sum_{i=1}^{i=a}(\mathrm{R2}_i - \mathrm{R1}_i)}{\sum_{i=1}^{i=a}\mathrm{R1}_i} \times 100\%, \tag{2}$$

where $\overline{\mathrm{R1}}$ and $\overline{\mathrm{R2}}$ are the mean rain rate from PR and GPROF2010, respectively.

d. Total error decomposition

To consider rainfall occurrence and intensity at the same time, a total error component analysis is adopted (Tian et al. 2009). The total error can be decomposed into three independent components: hit bias, miss bias, and false bias. Following the symbols in Tian et al. (2009), this study uses E, H, M, and F to represent the total error, hit bias, miss bias, and false bias, respectively. The total error and its three independent components have the relation $E = H - M + F$.

The total error is computed as the average difference between the TMI retrievals and the PR observations. For example, we again use $\mathrm{R1}_i$ and $\mathrm{R2}_i$ to represent the rain rates from PR and TMI ($i = 1, \ldots, N$, and $N = a + b + c + d$). Then the averaged total error is computed as

$$E = \frac{1}{N}\sum_{i=1}^{i=N}(\mathrm{R2}_i - \mathrm{R1}_i) = \frac{1}{N}\sum_{i=1}^{i=N}\mathrm{R2}_i - \frac{1}{N}\sum_{i=1}^{i=N}\mathrm{R1}_i. \tag{3}$$

The terms $1/N\sum_{i=1}^{i=N}\mathrm{R1}_i$ and $1/N\sum_{i=1}^{i=N}\mathrm{R2}_i$ are often referred to as unconditional mean rain rate of PR and TMI, respectively.

For the hit, miss, and false biases, Eq. (3) only applies to data in the corresponding category. For example, to compute the hit bias, we use the following equation:

$$H = \frac{1}{N}\sum_{i=1}^{i=a}(\mathrm{R2}_i - \mathrm{R1}_i), \tag{4}$$

where a is the hit number. It is clear that the hit bias is a measure of the intensity difference between PR and TMI based on the rainfall occurrence number (the hit number a) in the hit category. The correct negative category does not contribute to the total error because the rainfall intensity in that category is 0. These four numbers (E, H, M, and F) are expressed in units of millimeters per day ($\mathrm{mm\,day^{-1}}$). The hit bias H, miss bias M, and false bias F should not be confused with the mean bias in each category. Instead, they are essentially the summation of the difference between PR and TMI in the corresponding categories, normalized by the total sample size.

5. Results and discussions

a. Rainfall detection performance

Figure 1 shows the hit, miss, false, and correct negative number as percentages of the total observation numbers over land, coast, and ocean. Following discussion also includes POD and FAR values (Table 2). Note that the

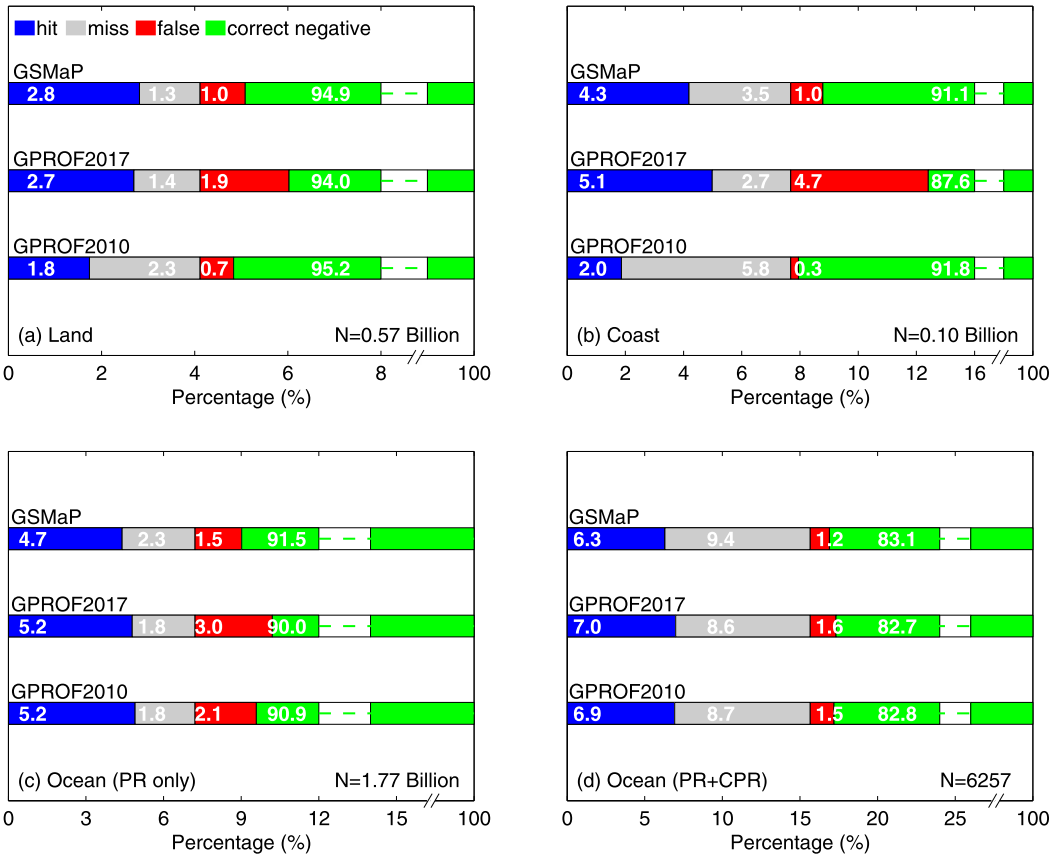

FIG. 1. The hit, miss, false, and correct negative numbers, expressed as the percentage of the total pixel number N over (a) land, (b) coast, and (c),(d) ocean. The total pixel number N is shown in the bottom-right corner of each panel. Over ocean, PR is taken as the reference in (c), and both PR and CPR are used in (d). Due to the much larger percentage of correct negative, only a small portion of it is shown in each subplot. The color schemes for hit, miss, false, and correct negative are shown in (a).

sum of the hit and miss numbers is the total raining pixel number according to the reference (e.g., PR), and the sum of the false alarm and correct negative numbers is the total nonraining pixel number.

Over land, GSMaP and GPROF2017 present similar hit numbers of 2.8% and 2.7%, respectively, for a total observation number of $N = 0.57$ billion. Both numbers are much larger than that from GPROF2010 at 1.8% (Fig. 1a). As a result, POD values from GSMaP and GPROF2017 are 65.45% and 68.39%, which are much larger than that from GPROF2010, 42.31% Table 2. On the other hand, GPROF2010 presents the smallest false alarm number (0.7%) and the largest correct negative number (95.2%).

TABLE 2. POD, FAR, and HSS for GPROF2010, GPROF2017, and GSMaP. Over land and coast, TRMM PR is taken as the reference. Over ocean, we also include *CloudSat* CPR observations as the reference. These statistics are computed at the pixel resolution and N is the total pixel number.

Dataset	POD (%)	FAR (%)	HSS	POD (%)	FAR (%)	HSS
	Land ($N = 0.57$ billion)			Coast ($N = 0.10$ billion)		
GPROF2010	42.31	0.75	0.51	24.29	0.29	0.36
GPROF2017	65.45	1.99	0.60	64.96	5.13	0.53
GSMaP	68.39	1.01	0.70	54.56	1.20	0.62
	Ocean (PR only, $N = 1.77$ billion)			Ocean (PR + CPR, $N = 6257$)		
GPROF2010	74.75	2.55	0.69	37.40	0.73	0.47
GPROF2017	73.21	3.22	0.66	36.56	1.20	0.45
GSMaP	67.85	1.94	0.68	33.31	0.63	0.45

These rainfall detection characteristics are caused by the different detection methods over land. As mentioned previously, GPROF2010 primarily uses a threshold value of 8 K between V21 and V85 for rainfall screening over land (Wang et al. 2009). The varying threshold values, either in the latitude–longitude grid box for each month from GSMaP or in the environmental-parameter binned intervals from GPROF2017, result in much larger POD values, compared with GPROF2010. However, the varying threshold values in GPROF2017 and GSMaP also falsely identify more raining pixels (larger FAR) than GPROF2010. Overall detection performance is evaluated using the HSS value (Table 2). As expected, both GPROF2017 and GSMaP have better overall detection performance indicated by the larger HSS values than GPROF2010 due to the varying threshold values. Further, the larger HSS value of 0.70 from GSMaP is most likely because it uses more regional information, compared with the HSS being 0.60 from GPROF2017.

Similarly, both GPROF2017 and GSMaP have much larger hit numbers over coast compared to GPROF2010 (Fig. 1b). However, GPROF2010 has a much smaller false alarm number of 0.3%, compared with 4.7% and 1.0% from GPROF2017 and GSMaP, respectively. Overall, GPROF2010 has a much smaller HSS value of 0.36 (Table 2), compared with 0.53 and 0.62 from GPROF2017 and GSMaP, respectively. The poor performance of GPROF2010 is because the detection approach from GPROF2010 is ad hoc in nature (simply extending the land algorithm to coast).

Over ocean, the detection statistics are first computed by using PR as the reference. Then, CPR observations are included into the detection assessment process. Regardless of the reference, all three datasets perform similarly as indicated by the similar numbers in Figs. 1c and 1d, and the similar accuracy metrics in Table 2. For example, the HSS values are ~0.70 (~0.45) for all three datasets when PR (CPR) is considered as the reference.

b. *Seasonal variation of detection performance*

For the analysis in this section, the data were separated into the Northern and Southern Hemispheres with the purpose of showing the detection performance in warm and cold seasons. However, only results for the Northern Hemisphere are shown since similar features were found in the Southern Hemisphere.

Figures 2a–c show the seasonal variations of POD, FAR, and HSS over land from GPROF2010, GPROF2017, and GSMaP. POD values from all three datasets are larger in the warm season (April–October) than in the cold season. Further analysis indicates that ice water path and storm top heights (Fig. 3) are larger in the warm season due to increased convection, resulting in a larger TB depression and larger POD. This property propagates into the level-3 gridded datasets and has been noted by many previous studies (e.g., Maggioni et al. 2016). More importantly, POD values from GSMaP (green curve in Fig. 2a) and GPROF2017 (red curve) are consistently larger than those from GPROF2010 (blue curves). As discussed previously, the varying threshold values in GSMaP and GPROF2017 account for the consistently larger POD values. The HSS values from GPROF2017 have a much smaller seasonal variation, and remain at ~0.58 throughout all months (Fig. 2c). In contrast, HSS values from GPROF2010 have a very strong seasonal variation, increasing from ~0.3 in January to ~0.5 in summer. In addition, GSMaP's HSS values also exhibit seasonal variation, with values ranging from ~0.5 in the cold season to ~0.7 in the warm season.

Due to the ad hoc nature of the GPROF2010 coastal algorithm, the POD values in all seasons are less than 40% (Fig. 2d), while POD values from GPROF2017 and GSMaP are consistently ~20%–40% larger than those from GPROF2010. The FAR values from GPROF2010 and GSMaP remain less than 2% in all months, while FAR values from GPROF2017 increase to ~7% in summer. Similar to the performance over land, HSS from GPROF2017 and GSMaP are consistently larger than from GPROF2010 in all months.

Over ocean, POD values from both GPROF2010 and GPROF2017 remain at ~75% in all months (Fig. 2g). In contrast, POD values from GSMaP have relatively larger seasonal variations, ranging from ~60% in January to ~75% from June to October. As discussed previously, GPROF2010 and GPROF2017 often falsely identify more rainfall occurrence. Therefore, FAR values from them are larger than those from GSMaP in most months (Fig. 2h). For HSS, the performance of these three datasets is similar, with the HSS difference among them being less than 0.05 in all months (Fig. 2i).

c. *Geospatial distribution of the detection performance*

This section analyzes the geospatial variation of rainfall detection performance in each 1° grid box over land and ocean (but not over coastal regions where the sample size is too limited). We intentionally separate the figures into land and ocean because of the very different variation ranges.

GPROF2010 presents smaller POD and FAR values over land compared with GSMaP (Figs. 4d,i), with exceptions for FAR over some areas in the Tibetan Plateau region. In terms of HSS, GSMaP performs

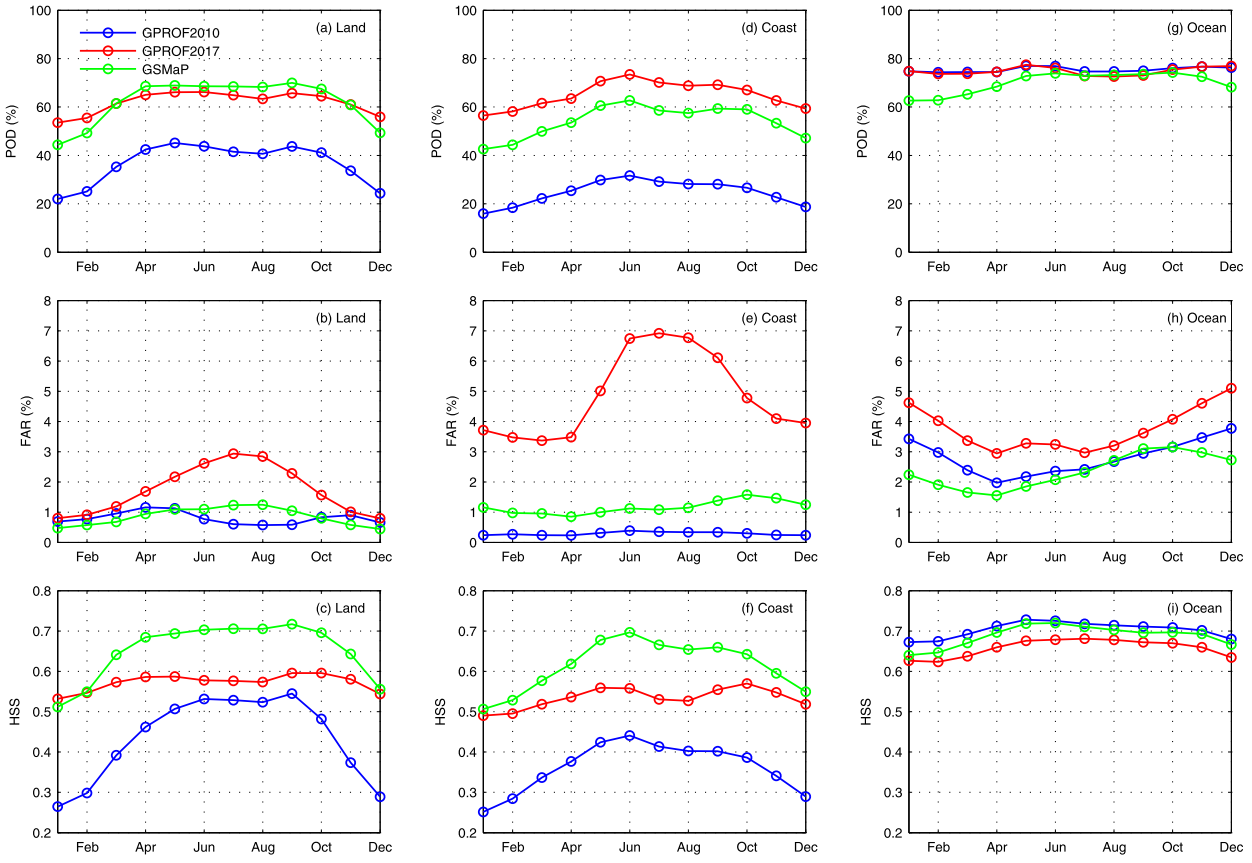

FIG. 2. (a)–(c) The seasonal variation of POD, FAR, and HSS in the Northern Hemisphere (NH) over land for GPROF2010, GPROF2017, and GSMaP. The line color for each product is shown in (a). (d)–(f) As in (a)–(c), but over coast. (g)–(i) As in (a)–(c), but over ocean. Data in 1997, 2014, and 2015 are not included in the seasonal analysis because data in certain months are not available.

better in the whole TRMM-covered region. Values of HSS from GSMaP are about 0.3 greater than those from GPROF2010 over arid regions (Fig. 4n; e.g., Sahara Desert and Arabian Peninsula). Comparing GPROF2017 with GSMaP, the most notable feature is that GPROF2017 has larger FAR values over central Africa, northern South America, and much of southern Asia (Fig. 4j). For HSS, GSMaP performs better in most of the TRMM region, except over some arid areas (Fig. 4o; e.g., Iranian Plateau). The better detection performance from GSMaP is most likely because it considers more regional feature by screening precipitation in each 1° grid box.

Similar to the overall detection performance in the Table 2, all three datasets have much more similar

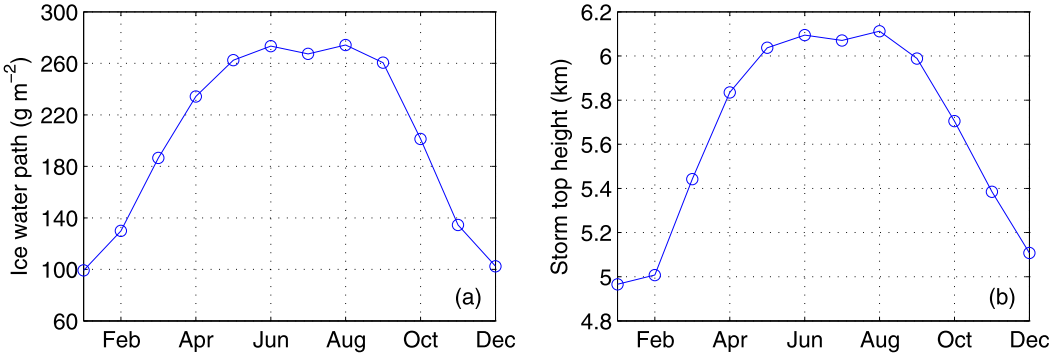

FIG. 3. (a) The monthly average ice water path over land in the Norther Hemisphere from January to December. Data is from January 1998 to December 2013. (b) As in (a), but for storm top height.

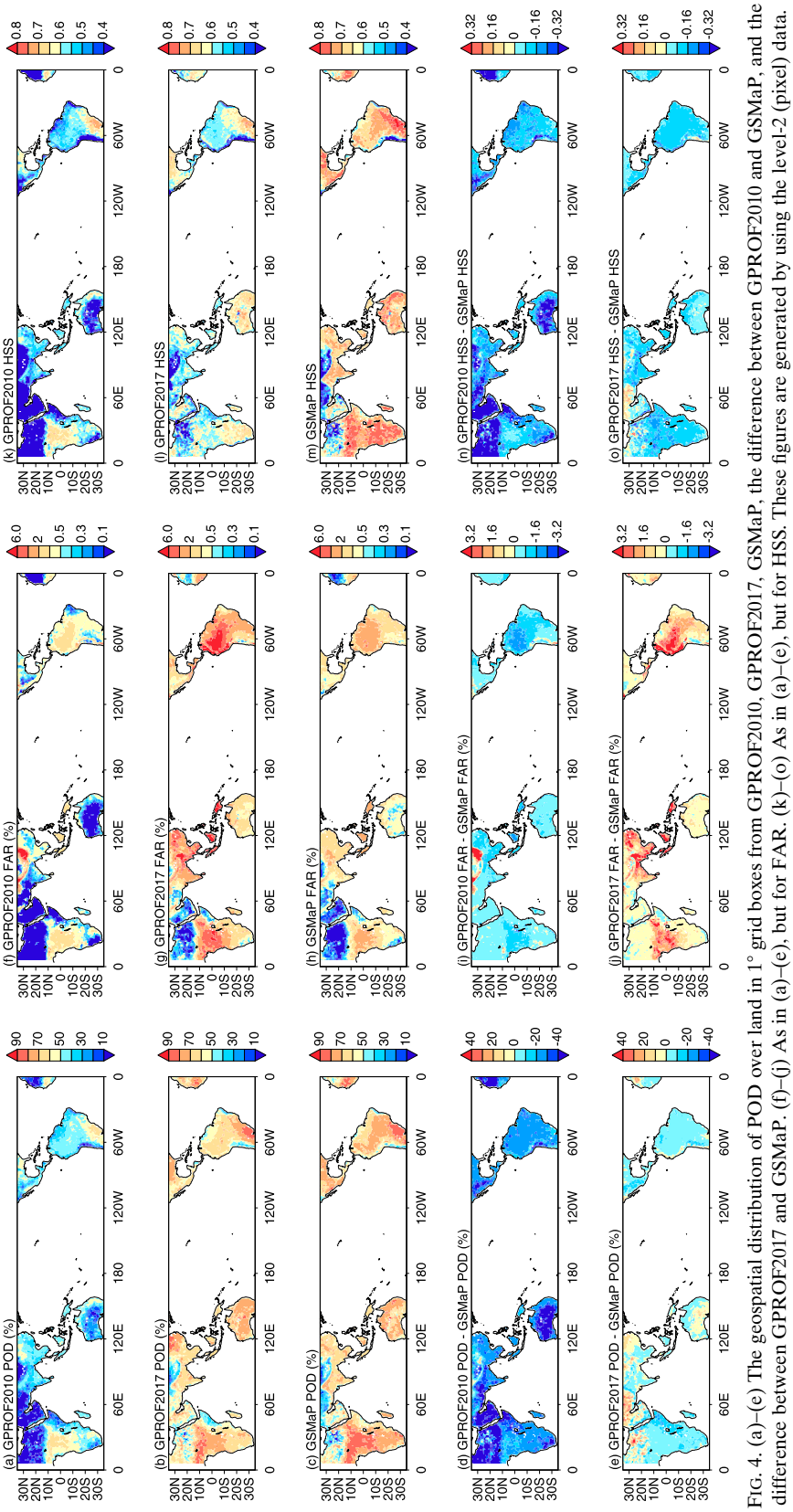

FIG. 4. (a)–(e) The geospatial distribution of POD over land in 1° grid boxes from GPROF2010, GPROF2017, GSMaP, the difference between GPROF2010 and GSMaP, and the difference between GPROF2017 and GSMaP. (f)–(j) As in (a)–(e), but for FAR. (k)–(o) As in (a)–(e), but for HSS. These figures are generated by using the level-2 (pixel) data.

geospatial distribution of POD, FAR, and HSS over oceans (Fig. 5) compared with over land. A noticeable feature is that both versions of GPROF tend to have larger POD and FAR values in light-rainfall-dominant regions (e.g., west of California and Peru coast; Figs. 5d,e,i,j). These features mean that both versions of GPROF correctly detect more raining pixels in these regions, but at the same time they also falsely identify more nonraining pixels as raining pixels in these regions.

d. Rainfall intensity estimate performance

This section analyzes rainfall intensity in the hit, false, and miss categories. In the hit category, three statistical metrics (CC, RMSE, and RB) are computed between PR and each TMI rainfall dataset. For the pixels in the false category (i.e., TMI retrieval results falsely identify nonraining pixels as raining pixels), we show their intensity distributions from each TMI rainfall dataset. In the miss category (i.e., TMI retrieval results fail to detect rainfall from PR), we show their intensity distribution from PR.

1) RAINFALL INTENSITY ANALYSIS IN THE HIT CATEGORY

Over land, a pronounced feature of the rainfall scatterplots is that GPROF2010 slightly over estimates convective rainfall intensity, while GPROF2017 and GSMaP (cf. Fig. 6a and Fig. 6b, and Fig. 6a and Fig. 6c) underestimate convective rainfall. Indeed, RB from GPROF2010 is 4.33% compared with −86.91% from GPROF2017 and −29.86% from GSMaP (Table 3). The small overestimation from GPROF2010 for convective rainfall implies that a convective–stratiform separation method is necessary in future rainfall retrieval algorithms since only GPROF2010 has explicitly implemented a convective–stratiform separation scheme in the intensity estimation process. Further, both GPROF2017 and GSMaP have larger CCs of 0.53 and 0.62, compared with 0.31 from GPROF2010. The largest possible rain rates in GPROF2010 and GPROF2017 are ~64 and ~100 mm h^{-1} (y axis in Figs. 6a and 6b), while it is 300 mm h^{-1} from GSMaP (Fig. 6c). For stratiform rainfall over land, all three datasets tend to overestimate light to moderate rain rates (<5 mm h^{-1}). This overestimation is more evident in GPROF2017 and GSMaP (Figs. 6e,f). In contrast, all three datasets significantly underestimate heavier rainfall (>16 mm h^{-1}). Furthermore, no single dataset performs best according to all three statistical metrics (CC, RMSE, and RB; Table 3).

As mentioned previously, GPROF2010 produces rain rates over coasts in an ad hoc fashion by simply extending the land algorithm to the coastal regions. As a result, for both convective and stratiform rainfall systems, rain rates from GPROF2010 only vary from ~1 to ~48 mm h^{-1} (Figs. 7a,d). Interestingly, the 2 mm h^{-1} rain rates for stratiform rainfall from GPROF2010 (Fig. 7d) generally correspond to lighter PR rain rates from 0.2 to 2 mm h^{-1} in PR observations. This feature contributes to the overall positive bias of 62.87% in GPROF2010 (Table 3). The dynamic range of the convective rain rates from GPROF2017 over coast is more reasonable with minimum values < 0.2 mm h^{-1} (Fig. 7b), compared with GPROF2010. However, rain rates from GPROF2017 are mostly under the 1-to-1 line, indicating a large underestimation. Indeed, GPROF2017 has the largest negative RB of −98.43% for convective rainfall over coast, compared with RB of −69.63% from GPROF2010, and −51.88% from GSMaP (Table 3). For stratiform rainfall over coasts, the most noticeable feature is that GSMaP performs the best in term of the distribution in Fig. 7f and all three statistical metrics. Specifically, stratiform rainfall over coasts from GSMaP has the largest CC of 0.66, the smallest RMSE of 1.05 mm h^{-1}, and the smallest RB of −6.43% (Table 3).

The differences between these three datasets are much smaller over ocean compared with over land and coast. In particular, GPROF2010 and GPROF2017 show very similar characteristics, both on the scatterplots (cf. Fig. 8a and Fig. 8b, and cf. Fig. 8d and Fig. 8e) and in terms of the statistical metrics, as shown in Table 3.

To summarize, we show that over land these three datasets differ greatly. GPROF2010 shows a much weaker correlation, compared with the other two products. However, it also has a much smaller relative bias value under the convective scenario. Over coast, GSMaP performs the best in terms of all three statistical metrics for stratiform rainfall. Over ocean, the differences between them are much smaller and GPROF2017 performs the best in terms of all three statistical metrics for convective rainfall. One common feature over ocean is that all three datasets greatly underestimate convective rainfall intensity.

2) RAINFALL INTENSITY ANALYSIS IN THE FALSE AND MISS CATEGORIES

This section analyzes the rainfall intensity distribution in the false and miss categories. Small rain rates in both categories mean better performance because nonzero rain rates in the false category mean that TMI falsely identifies rainfall while PR indicates otherwise, and rain rates in the miss category mean that TMI misses the rainfall indicated by PR.

Figure 9a shows the rainfall occurrence histograms in the false category for GPROF2010 (blue), GPROF2017

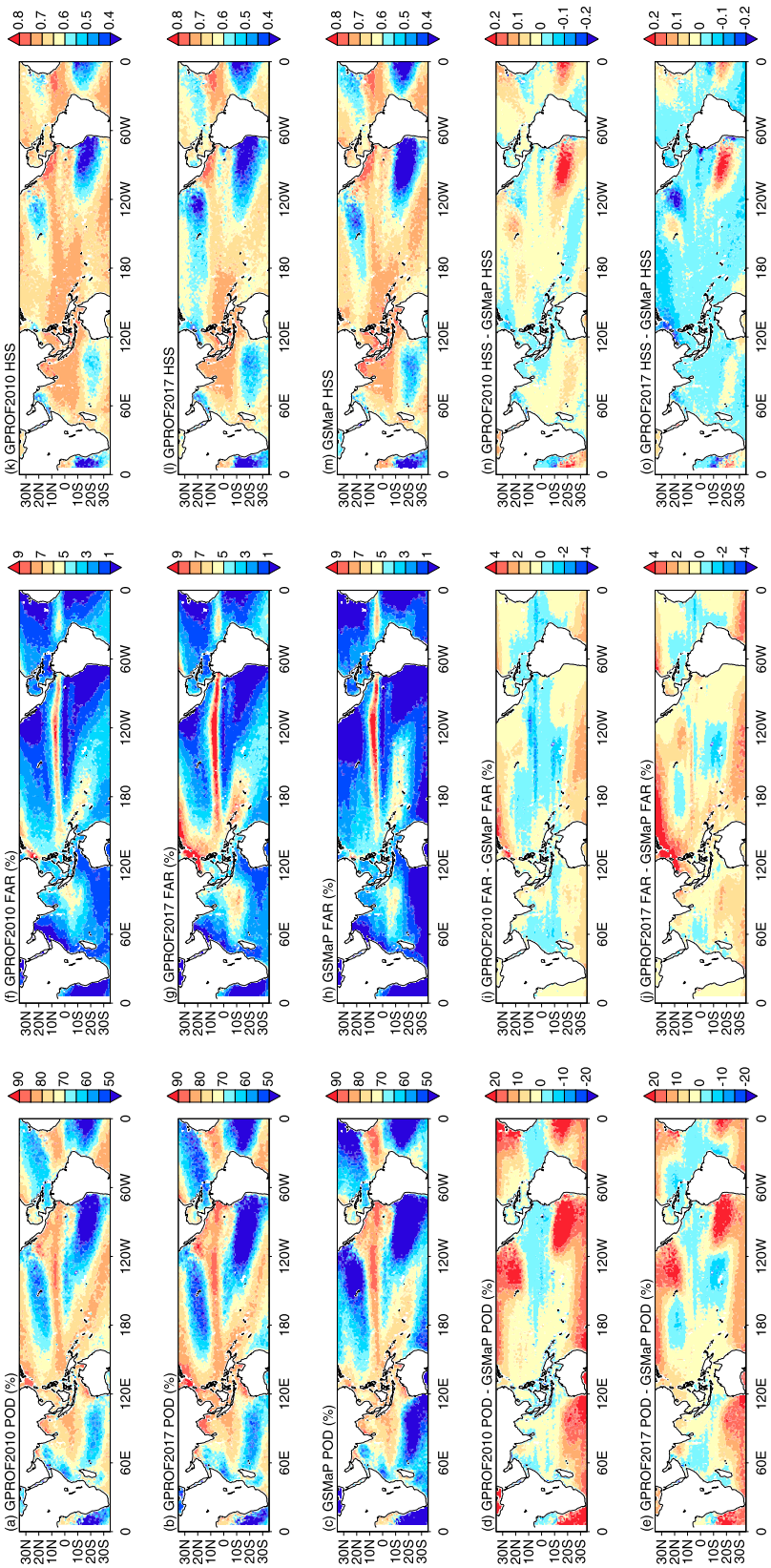

FIG. 5. As in Fig. 4, but over ocean.

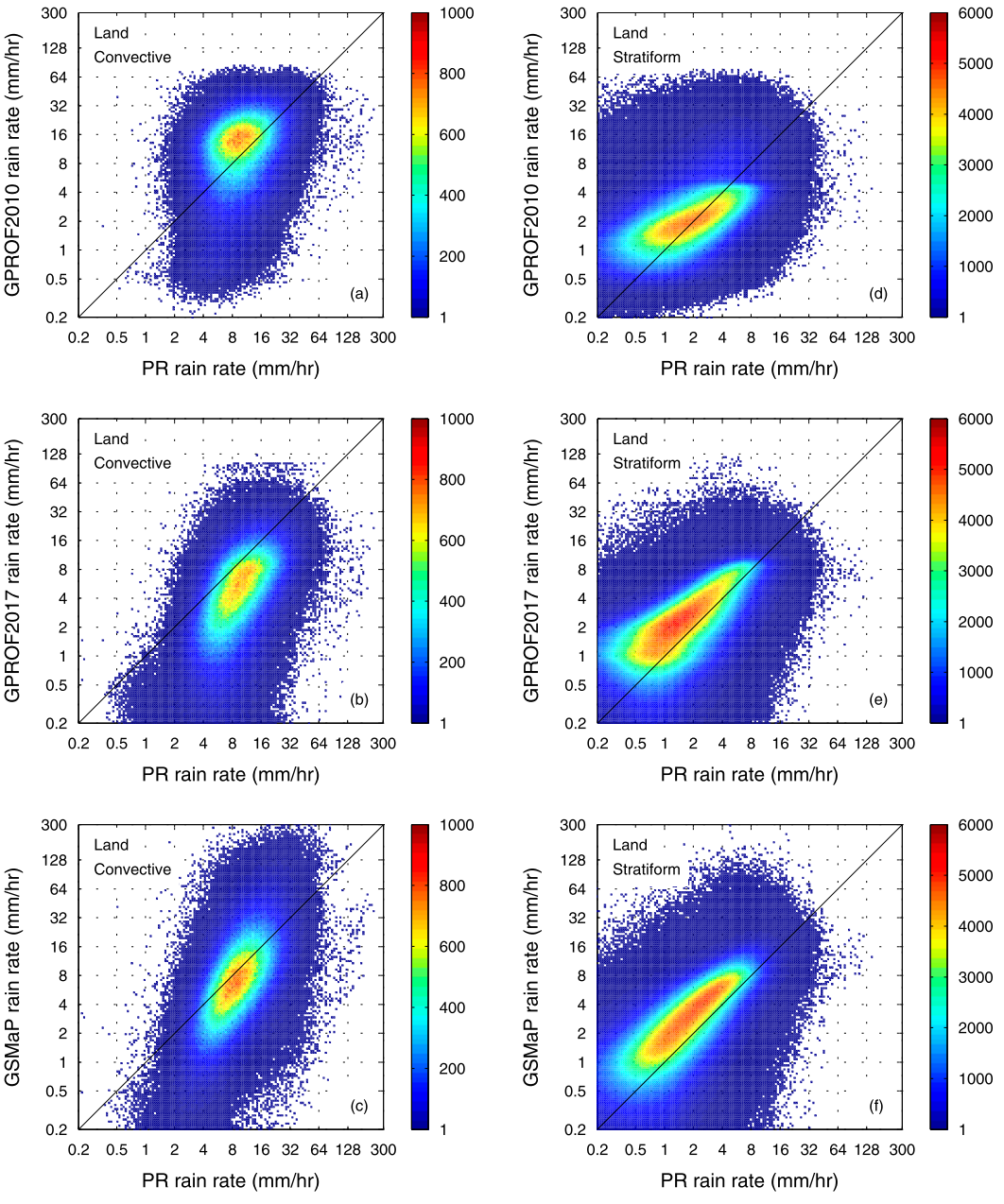

FIG. 6. (a)–(c) Scatterplots between rain rates from GPROF2010 and from PR, between rain rates from GPROF2017 and from PR, and between rain rates from GSMaP and from PR, for convective rainfall over land. (d)–(f) As in (a)–(c), but for stratiform rainfall.

(red), and GSMaP (green) over land. Clearly, GPROF2010 has a larger peak around 2 mm h^{-1} compared with 0.1 mm h^{-1} from GPROF2017 and GSMaP, indicating that GPROF2010 tends to falsely identify heavier rainfall than GPROF2017 and GSMaP. Particularly, GPROF2010 shows a larger percentage of falsely identified rainfall heavier than 4 mm h^{-1}. Further analysis suggests that these falsely identified rainfall pixels are often near the edges of convective rainfall systems and are classified as ''convective'' pixels by GPROF2010. Therefore, GPROF2010 produces large rain rates for these falsely identified convective pixels. Over coasts, about 35% of falsely identified rain rates from GPROF2010 are ~2 mm h^{-1} (Fig. 9b). In contrast, GPROF2017 and GSMaP tend to have smaller rain rates in the false category, similar to over land. Over ocean, falsely identified rainfall tends to have a larger rainfall intensity from GSMaP and the lowest values from GPROF2010.

TABLE 3. CC, RMSE, and RB from convective and stratiform rainfall in the hit category for GPROF2010, GPROF2017, and GSMaP at the pixel resolution.

Surface type/rain type	Dataset	CC	RMSE (mm h^{-1})	RB (%)
Land/convective	GPROF2010	0.31	0.86	4.33
	GPROF2017	0.53	1.27	−86.91
	GSMaP	0.62	0.91	−29.86
Land/stratiform	GPROF2010	0.51	1.06	34.79
	GPROF2017	0.57	1.08	34.40
	GSMaP	0.66	1.06	42.69
Coast/convective	GPROF2010	0.36	1.01	−51.88
	GPROF2017	0.66	1.34	−98.43
	GSMaP	0.71	1.35	−69.63
Coast/stratiform	GPROF2010	0.46	1.19	62.87
	GPROF2017	0.51	1.20	54.45
	GSMaP	0.66	1.05	−6.43
Ocean/convective	GPROF2010	0.77	0.95	−63.35
	GPROF2017	0.86	0.67	−42.59
	GSMaP	0.84	0.78	−53.08
Ocean/stratiform	GPROF2010	0.80	0.75	15.09
	GPROF2017	0.83	0.70	32.08
	GSMaP	0.77	0.83	7.13

For the rain rates in the miss category, the differences between these products and over all surface types are small (Figs. 9d–f). These histograms all peak around 0.02 mm h^{-1}.

e. Total error decomposition

This section first shows the overall unconditional mean rain rate from PR, GPROF2010, GPROF2017, and GSMaP over three surface types. Then the total error E and its three independent components (the hit bias H, the miss bias M, and the false bias F) from these three TMI rainfall datasets are analyzed. One should recall that the total error E in Eq. (3) is the overall unconditional mean rain rate difference between a TMI rainfall dataset (e.g., GPROF2010) and the reference (e.g., PR). Finally, geospatial distribution of the total error and its three components in 1° grid boxes is analyzed for these three datasets.

1) OVERALL UNCONDITIONAL MEAN RAIN RATE

Figure 10 shows the overall unconditional mean rain rate over land, coast, and ocean from PR and the three TMI products. Over land, the mean rain rate is 1.89, 2.12, 1.72, and 2.13 mm day^{-1} from PR, GPROF2010, GPROF2017, and GSMaP, respectively. Obviously, GPROF2017 underestimates the mean rain rate, while GPROF2010 and GSMaP overestimate the mean rain rate. Over coast, GPROF2017 produces a mean rain rate that is much closer to the mean rain rate from PR compared with those from GPROF2010 and GSMaP. Over ocean, the differences between these three datasets are much smaller compared with PR.

Interestingly, the overall unconditional mean rain rate from PR is 3.39 mm day^{-1} over coast, which is much larger than those over ocean (2.69 mm day^{-1}) and over land (1.89 mm day^{-1}). This is consistent with the study by Ogino et al. (2016), which showed that precipitation amount peaks around the coastline. They concluded that the diurnal land–sea circulation is primarily responsible for the coastal precipitation maximum, compared with precipitation amount over land and ocean.

2) TOTAL ERROR AND ITS THREE COMPONENTS

The total error and its three independent components are analyzed in this section (Table 4). These four values (E, H, M, and F) are also shown as a percentage of the unconditional mean rain rate from PR.

Over land, GPROF2010 and GSMaP have very similar total bias (E in Table 4, 0.23 and 0.24 mm day^{-1}, respectively). However, bias decomposition analysis reveals a very different picture. All three components for GPROF2010 are larger than those for GSMaP, which means that GPROF2010 has larger hit, miss, and false biases, which partially cancel each other, leading to an unconditional mean rain rate similar to GSMaP. The larger false bias is primarily caused by the larger false rain rate intensities in GPROF2010 (Fig. 9a), while the large miss bias is primarily caused by the large miss rainfall occurrence (Fig. 1a). GPROF2017 has a negative total bias of −0.17 mm day^{-1}, compared with a positive total bias from both GPROF2010 and GSMaP. This negative total bias is partially caused by the large negative hit bias due to the large underestimation of convective rainfall in GPROF2017 (Fig. 6b).

Over coast, GPROF2017 has the smallest total bias of 0.05 mm day^{-1}, followed by the total bias of −0.34 mm day^{-1} from GSMaP, and −1.12 mm day^{-1} from GPROF2010. Further analysis shows that the small total bias from GPROF2017 primarily results from the cancellation of the miss and false biases. The large total bias from GPROF2010 is caused by the large miss bias of −1.62 mm day^{-1}, which is very large because it is 47.87% of the unconditional mean rain rate of PR over coast (3.39 mm day^{-1}).

The very large miss bias from GPROF2010 may seem contradictory with the intensity histogram in Fig. 9d, where all three datasets show similar miss rainfall intensity. In fact, this result is because GPROF2010 has a much larger miss number (Fig. 1b, 5.8% versus 2.7% from GPROF2017 and 3.5% from GSMaP). According to Eq. (4), the bias computation is essentially the summation of the rain rate in each category, which includes both occurrence and intensity information (hence, the presentation of rainfall occurrence in Fig. 1 and rainfall intensity distribution in Fig. 9). Also, GPROF2010 has

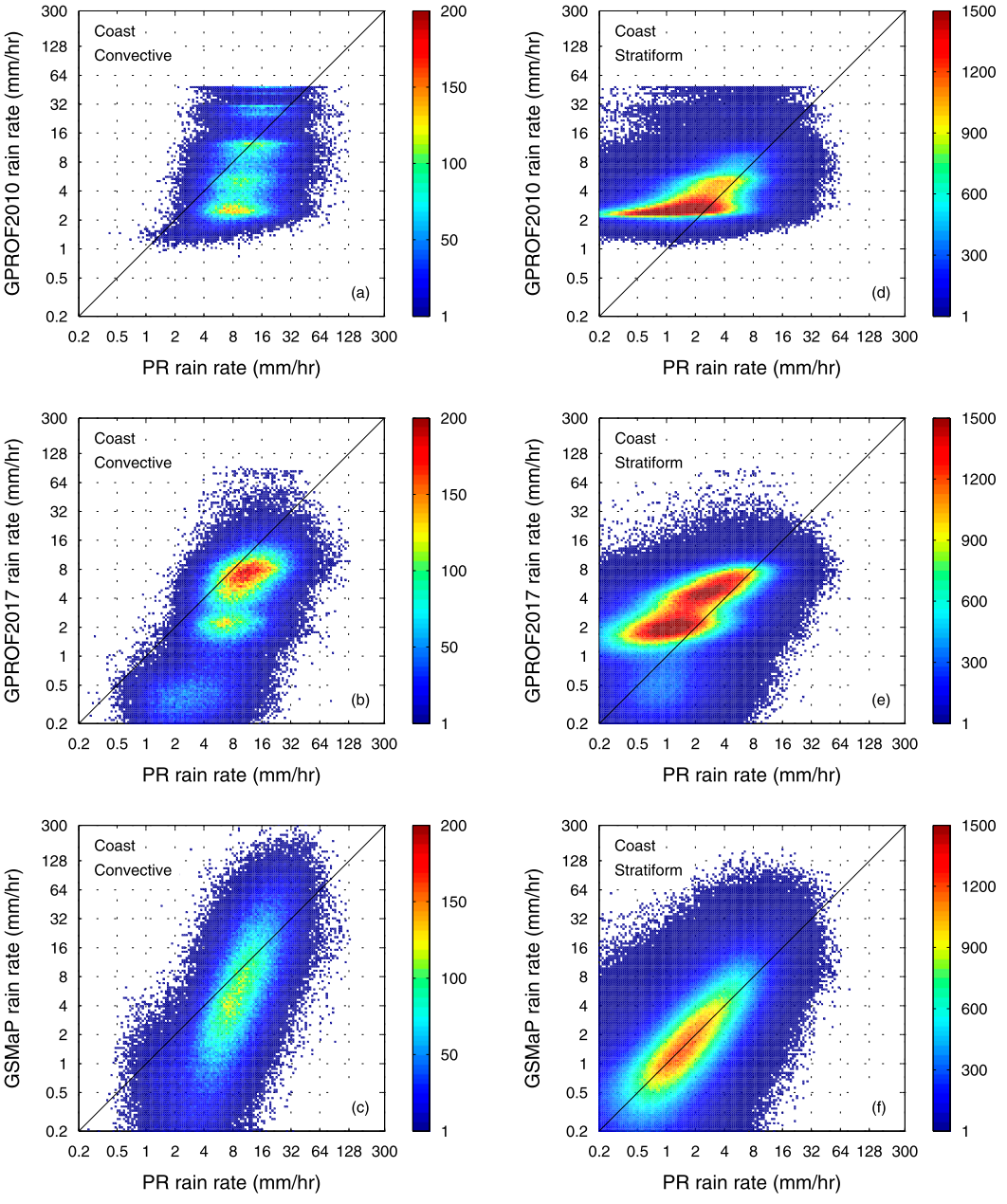

FIG. 7. (a)–(c) Scatterplots between rain rates from GPROF2010 and from PR, between rain rates from GPROF2017 and from PR, and between rain rates from GSMaP and from PR, for convective rainfall over coast. (d)–(f) As in (a)–(c), but for stratiform rainfall.

the smallest false bias compared with GPROF2017 and GSMaP, although Fig. 9a shows that GPROF2010 tends to have a larger false rain intensity (peaking around $2\,\mathrm{mm\,h^{-1}}$). This result is because GPROF2010 falsely identifies the least amount of rainfall occurrence over the coastal region (Fig. 1b, 0.3% from GPROF2010 versus 2.7% from GPROF2017 and 3.5% from GSMaP).

The differences in the total bias are relatively smaller over ocean compared with over land and coast (Table 4). One pronounced feature is that both GPROF versions have larger false bias components than GSMaP caused by larger false rainfall occurrence (Fig. 1c), although GSMaP tends to have larger false rainfall intensities (Fig. 9c).

3) GEOSPATIAL DISTRIBUTION OF TOTAL ERROR AND ITS THREE COMPONENTS OVER LAND

This section shows the geospatial distribution of the total error and its three components from the three TMI

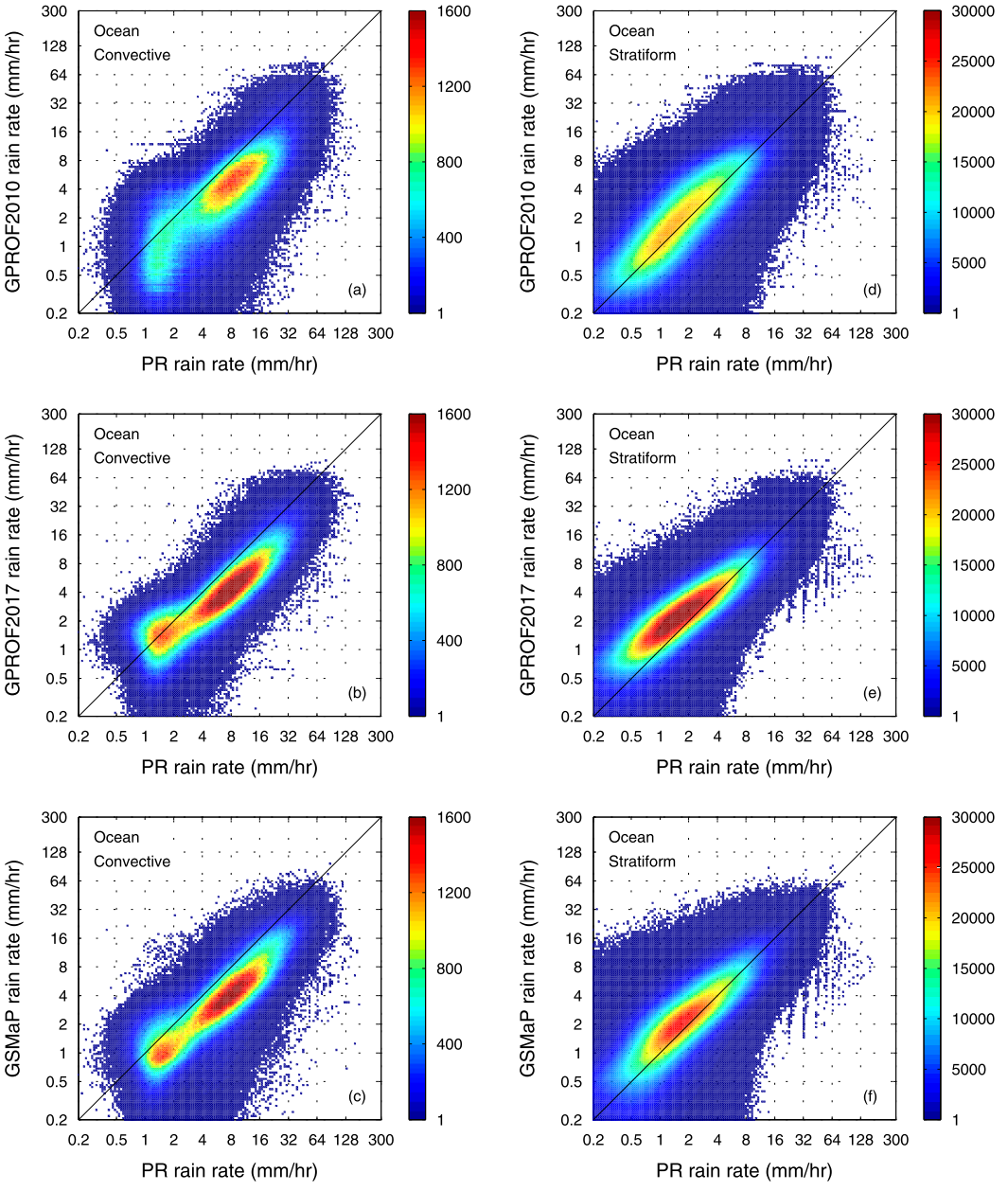

FIG. 8. (a)–(c) Scatterplots between rain rates from GPROF2010 and from PR, between rain rates from GPROF2017 and from PR, and between rain rates from GSMaP and from PR, for convective rainfall over ocean. (d)–(f) As in (a)–(c), but for stratiform rainfall.

rainfall datasets over land. Similar analysis has also been done over ocean without noticing clear difference (not shown).

The total error and its three components have evident differences between the three datasets in several regions (Fig. 11). First, GPROF2010 has a larger positive total error in central Africa (Fig. 11a) compared with GPROF2017 (Fig. 11e) and GSMaP (Fig. 11i). Different bias components account for this positive total error over central Africa. This positive bias in GPROF2010 is primarily caused by the large positive hit bias (Fig. 11b). Precipitation systems in this region are often associated with very deep convection and therefore are associated with larger ice water path (Zipser et al. 2006; You and Liu 2012). The higher ice water path leads to large hit biases in GPROF2010 since the same equations for rainfall intensity estimation are applied globally. In contrast, both GPROF2017 and

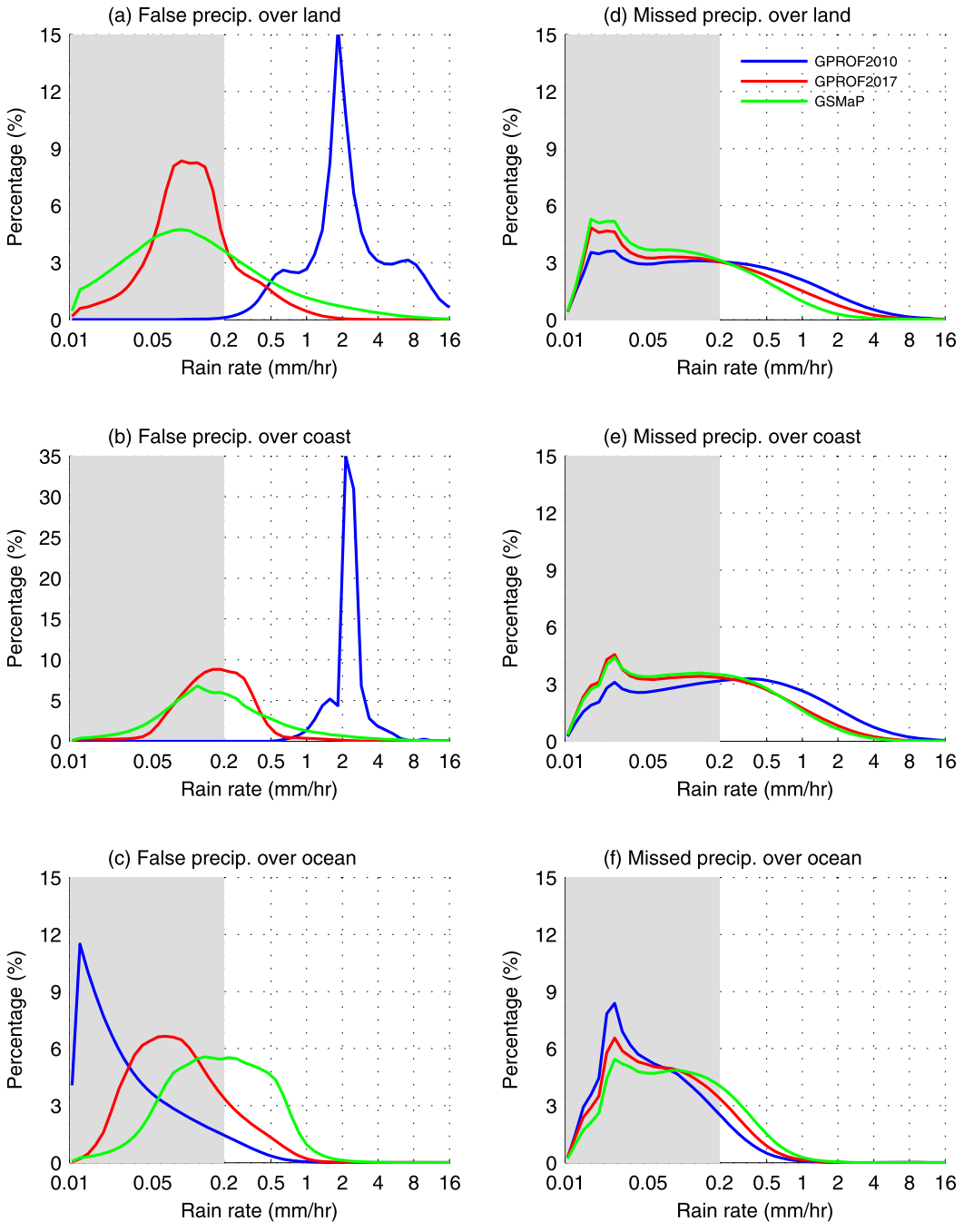

FIG. 9. Rainfall intensity distribution for GPROF2010, GPROF2017, and GSMaP in the false and miss categories over (a),(d) land, (b),(e) coast, and (c),(f) ocean. The line color for each dataset is shown in (d). The area of rainfall intensity less than 0.2 mm h^{-1} is lightly shaded. Rainfall intensity less than 0.2 mm h^{-1} is assigned as 0 in the detection- and intensity-related computation.

GSMaP establish different relationships between rain rate and TB depending either on regions or on weather regimes, which lead to much smaller hit biases in this region (cf. Fig. 11b and Fig. 11f, cf. Fig. 11b and Fig. 11j). The larger false bias over central Africa from GPROF2017 (Fig. 11g; mainly due to the larger false detection number) contributes more to the positive total error in this region, compared with the hit bias in this region (Fig. 11f).

Second, the much larger positive total error over the Tibetan Plateau region in GPROF2010 (Fig. 11a) is mainly caused by the large false bias (Fig. 11c).

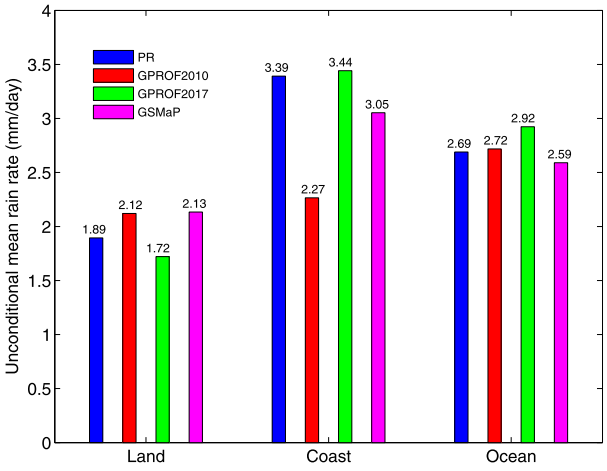

FIG. 10. Unconditional mean rain rate (mm day^{-1}) from PR, GPROF2010, GPROF2017, and GSMaP.

As discussed previously, the static detection threshold value in GPROF2010 is responsible for this larger false bias compared with GPROF2017 and GSMaP.

Third, both GPROF2010 and GPROF2017 have prevalent negative total error (Figs. 11a,e) over the northern Amazon region, while the total error in GSMaP over this region is generally positive. The error decomposition reveals that large miss biases are solely responsible for the prevalent negative total error over this region in GPROF2010 (Fig. 11d), while both negative hit biases and miss biases contribute to this feature in GPROF2017. For GSMaP, the dominant positive total error is mainly due to the positive hit bias in this region.

6. Conclusions

This study compares rainfall detection and intensity estimates from three TMI rainfall datasets (i.e., GPROF2010, GPROF2017, and GSMaP) using the full TRMM satellite record from December 1997 to April 2015. The analysis is separated into three surface types, including land, coast, and ocean. For rainfall intensity analysis in the hit category (i.e., both PR and TMI detect rainfall), we also separate rainfall systems into convective and stratiform components. TRMM PR is taken as the primary reference over all surface types, although *CloudSat* CPR observations have also been included over ocean. Key results are summarized as follows:

1) For detection performance, GPROF2017 and GSMaP show better performance than GPROF2010 as indicated by larger HSS values over both land and coast. The dynamical threshold values used in the rainfall detection process by GPROF2017 and GSMaP accounts for this better performance. It is further noticed that GSMaP has better detection capability than GPROF2017, which is most likely because GSMaP uses more regional information by screening rainfall over each 1° grid box, while GPROF2017 detects rainfall in different environmental-variable-binned databases (e.g., TPW and surface temperature). Over ocean, all three datasets perform similarly regardless of using PR or CPR as the reference. The seasonal and geospatial analyses of the detection performance metrics generally agree with the overall analysis.
2) For rainfall intensity over land, there is no clear superior dataset in terms of all three statistical metrics (CC, RMSE, and RB). However, both GPROF2017 and GSMaP have much better correlation values than GPROF2010 for convective rainfall over land, which result from the regionally dependent relation between brightness temperature and rain rate implemented in GPROF2017 and GSMaP. On the other hand, GPROF2010 only slightly overestimates convective rainfall over land compared with much larger underestimation from GPROF2017 and GSMaP, which is likely due to the convective–stratiform separation scheme in GPROF2010. It may imply the necessity to implement

TABLE 4. Total error E and its three independent components: hit bias H, miss bias M, and false alarm bias F over land, coast, and ocean for GPROF2010, GPROF2017, and GSMaP. These statistics are computed at the pixel resolution and also shown as the percentage of unconditional mean PR rain rate in parentheses.

Surface type	Dataset	H (mm day^{-1})	$-M$ (mm day^{-1})	F (mm day^{-1})	$E = H - M + F$ (mm day^{-1})
Land	GPROF2010	0.43 (22.49%)	−0.62 (−32.61%)	0.42 (22.04%)	0.23 (11.92%)
	GPROF2017	−0.14 (−7.20%)	−0.30 (−15.61%)	0.26 (13.64%)	−0.17 (−9.17%)
	GSMaP	0.27 (14.03%)	−0.21 (−11.14%)	0.18 (9.69%)	0.24 (12.59%)
Coast	GPROF2010	0.34 (10.06%)	−1.62 (−47.87%)	0.17 (4.61%)	−1.12 (−33.21%)
	GPROF2017	−0.02 (−0.52%)	−0.49 (−14.57%)	0.56 (16.55%)	0.05 (1.46%)
	GSMaP	0.08 (2.45%)	−0.62 (−18.15%)	0.19 (5.69%)	−0.34 (−10.01%)
Ocean	GPROF2010	−0.11 (−4.01%)	−0.05 (−1.78%)	0.18 (6.85%)	0.03 (1.07%)
	GPROF2017	0.11 (3.98%)	−0.11 (−4.00%)	0.23 (8.74%)	0.23 (8.72%)
	GSMaP	0.05(1.84%)	−0.23 (−8.61%)	0.08 (3.10%)	−0.10 (−3.67%)

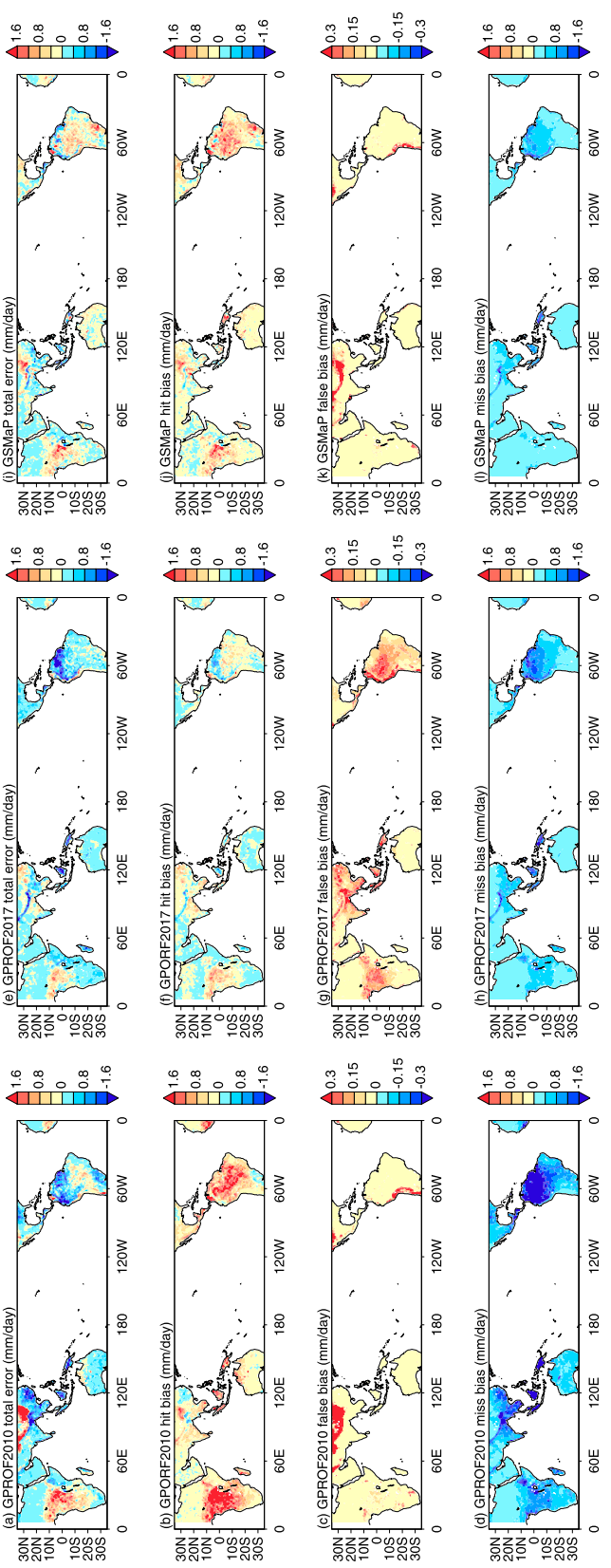

FIG. 11. (a)–(d) The total error and its three components from GPROF2010 over land in each 1° grid box. (e)–(h) As in (a)–(d), but from GPROF2017. (i)–(l) As in (a)–(d), but from GSMaP. These figures are generated by using the level-2 (pixel) data.

a convective–stratiform separation scheme in the retrieval process.

3) For rainfall intensity over coast, GSMaP performs the best for stratiform rainfall in terms of all three statistical metrics (CC, RMSE, and RB) and has the largest correlation for convective rainfall. This better performance from GSMaP is particularly evident in the scatterplots (Fig. 7). GSMaP's coastal rainfall retrieval algorithm considers the land–ocean percentage in each coastal pixel, which accounts for its better performance. In contrast, GPROF2010 extends the land algorithm over coast, resulting in a lack of continuity for the rainfall intensities. Although GPROF2017 has a coastal retrieval algorithm, it does not consider the land–ocean percentage for each pixel.
4) For rainfall intensity over ocean, the differences between these three datasets are much smaller than those over coast and land. This feature further confirms that rainfall retrieval algorithms over ocean rely on more direct relations between liquid water rain drops with surface rainfall rates, while rainfall is primarily estimated by the scattering signatures over land.
5) The error component decomposition analysis reveals that the large overall underestimation from GPROF2010 over coast is primarily caused by the miss bias. That is, GPROF2010 misses many more rainfall events over coastal regions compared with the other two datasets. The geospatial analysis shows that the positive total error over central Africa in GPROF2010 and GSMaP is primarily caused by positive hit bias, while false bias in GPROF2017 is largely responsible for positive total error in this region.

Finally, inhomogeneity within the large radiometer footprint (e.g., 20.9 km × 34.6 km at 19 GHz) can also cause large uncertainties for both precipitation detection and intensity estimates, which is especially challenging under convective rainfall situations. Future precipitation retrieval algorithms should also take the footprint inhomogeneity into consideration.

Acknowledgments. TRMM 2A12, 2A25, 2A23, and 2AGPROFTMI data are downloaded from NASA PPS website (https://storm.pps.eosdis.nasa.gov/storm/). JAXA TMI data are provided by JAXA Earth Observation Research Center (EORC). *CloudSat* data are downloaded at http://www.cloudsat.cira.colostate.edu/. The results of this paper are obtained pursuant to the Collaborative Research Agreement (Non-Funded) for the Precipitation Measuring Mission between JAXA and the University of Maryland for the 8th RA. We thank Dr. Jackson Tan for discussions on making Fig. 1.

REFERENCES

Aonashi, K., and Coauthors, 2009: GSMaP passive microwave precipitation retrieval algorithm: Algorithm description and validation. *J. Meteor. Soc. Japan*, **87A**, 119–136, https://doi.org/10.2151/jmsj.87A.119.

Chen, S., and Coauthors, 2013a: Evaluation and uncertainty estimation of NOAA/NSSL next-generation national mosaic quantitative precipitation estimation product (Q2) over the continental United States. *J. Hydrometeor.*, **14**, 1308–1322, https://doi.org/10.1175/JHM-D-12-0150.1.

——, and Coauthors, 2013b: Similarity and difference of the two successive V6 and V7 TRMM multisatellite precipitation analysis performance over China. *J. Geophys. Res. Atmos.*, **118**, 13 060–13 074, https://doi.org/10.1002/2013JD019964.

Ferraro, R. R., and G. F. Marks, 1995: The development of SSM/I rain-rate retrieval algorithms using ground-based radar measurements. *J. Atmos. Oceanic Technol.*, **12**, 755–770, https://doi.org/10.1175/1520-0426(1995)012<0755:TDOSRR>2.0.CO;2.

——, N. C. Grody, and G. F. Marks, 1994: Effects of surface conditions on rain identification using the DMSP-SSM/I. *Remote Sens. Rev.*, **11**, 195–209, https://doi.org/10.1080/02757259409532265.

——, E. A. Smith, W. Berg, and G. J. Huffman, 1998: A screening methodology for passive microwave precipitation retrieval algorithms. *J. Atmos. Sci.*, **55**, 1583–1600, https://doi.org/10.1175/1520-0469(1998)055<1583:ASMFPM>2.0.CO;2.

Figueroa, S. N., and Coauthors, 2016: The Brazilian Global Atmospheric Model (BAM): Performance for tropical rainfall forecasting and sensitivity to convective scheme and horizontal resolution. *Wea. Forecasting*, **31**, 1547–1572, https://doi.org/10.1175/WAF-D-16-0062.1.

Gopalan, K., N.-Y. Wang, R. Ferraro, and C. Liu, 2010: Status of the TRMM 2A12 land precipitation algorithm. *J. Atmos. Oceanic Technol.*, **27**, 1343–1354, https://doi.org/10.1175/2010JTECHA1454.1.

Hamada, A., Y. N. Takayabu, C. Liu, and E. J. Zipser, 2015: Weak linkage between the heaviest rainfall and tallest storms. *Nat. Commun.*, **6**, 6213, https://doi.org/10.1038/NCOMMS7213.

Haynes, J. M., T. S. L'Ecuyer, G. L. Stephens, S. D. Miller, C. Mitrescu, N. B. Wood, and S. Tanelli, 2009: Rainfall retrieval over the ocean with spaceborne W-band radar. *J. Geophys. Res.*, **114**, D00A22, https://doi.org/10.1029/2008JD009973.

Hirose, M., and K. Nakamura, 2004: Spatiotemporal variation of the vertical gradient of rainfall rate observed by the TRMM Precipitation Radar. *J. Climate*, **17**, 3378–3397, https://doi.org/10.1175/1520-0442(2004)017<3378:SVOTVG>2.0.CO;2.

Hou, A. Y., and Coauthors, 2014: The Global Precipitation Measurement mission. *Bull. Amer. Meteor. Soc.*, **95**, 701–722, https://doi.org/10.1175/BAMS-D-13-00164.1.

Huffman, G. J., and Coauthors, 2007: The TRMM Multisatellite Precipitation Analysis (TMPA): Quasi-global, multiyear, combined-sensor precipitation estimates at fine scales. *J. Hydrometeor.*, **8**, 38–55, https://doi.org/10.1175/JHM560.1.

Iguchi, T., T. Kozu, R. Meneghini, J. Awaka, and K. Okamoto, 2000: Rain-profiling algorithm for the TRMM precipitation radar. *J. Appl. Meteor.*, **39**, 2038–2052, https://doi.org/10.1175/1520-0450(2001)040<2038:RPAFTT>2.0.CO;2.

Joyce, R. J., J. E. Janowiak, P. A. Arkin, and P. Xie, 2004: CMORPH: A method that produces global precipitation

estimates from passive microwave and infrared data at high spatial and temporal resolution. *J. Hydrometeor.*, **5**, 487–503, https://doi.org/10.1175/1525-7541(2004)005<0487:CAMTPG>2.0.CO;2.

Kida, S., S. Shige, T. Kubota, K. Aonashi, and K. Okamoto, 2009: Improvement of rain/no-rain classification methods for microwave radiometer observations over the ocean using a 37 GHz emission signature. *J. Meteor. Soc. Japan*, **87A**, 165–181, https://doi.org/10.2151/jmsj.87A.165.

——, ——, T. Manabe, T. L'Ecuyer, and G. Liu, 2010: Cloud liquid water path for the rain/no-rain classification method over ocean in the GSMaP algorithm. *Trans. Japan Soc. Aeronaut. Space Sci. Aerosp. Technol. Japan*, **8**, 19–23, https://doi.org/10.2322/tastj.8.pn_19.

Kozu, T., and Coauthors, 2001: Development of precipitation radar onboard the Tropical Rainfall Measuring Mission (TRMM) satellite. *IEEE Trans. Geosci. Remote Sens.*, **39**, 102–116, https://doi.org/10.1109/36.898669.

Kubota, T., and Coauthors, 2007: Global precipitation map using satellite-borne microwave radiometers by the GSMaP Project: Production and validation. *IEEE Trans. Geosci. Remote Sens.*, **45**, 2259–2275, https://doi.org/10.1109/TGRS.2007.895337.

——, T. Ushio, S. Shige, S. Kida, M. Kachi, and K. Okamoto, 2009: Verification of high-resolution satellite-based rainfall estimates around Japan using a gauge-calibrated ground-radar dataset. *J. Meteor. Soc. Japan*, **87A**, 203–222, https://doi.org/10.2151/jmsj.87A.203.

Kummerow, C., W. Barnes, T. Kozu, J. Shiue, and J. Simpson, 1998: The Tropical Rainfall Measuring Mission (TRMM) sensor package. *J. Atmos. Oceanic Technol.*, **15**, 809–817, https://doi.org/10.1175/1520-0426(1998)015<0809:TTRMMT>2.0.CO;2.

——, and Coauthors, 2001: The evolution of the Goddard Profiling Algorithm (GPROF) for rainfall estimation from passive microwave sensors. *J. Appl. Meteor.*, **40**, 1801–1820, https://doi.org/10.1175/1520-0450(2001)040<1801:TEOTGP>2.0.CO;2.

Kummerow, C. D., S. Ringerud, J. Crook, D. Randel, and W. Berg, 2011: An observationally generated a priori database for microwave rainfall retrievals. *J. Atmos. Oceanic Technol.*, **28**, 113–130, https://doi.org/10.1175/2010JTECHA1468.1.

——, D. L. Randel, M. Kulie, N.-Y. Wang, R. Ferraro, S. Joseph Munchak, and V. Petkovic, 2015: The evolution of the Goddard profiling algorithm to a fully parametric scheme. *J. Atmos. Oceanic Technol.*, **32**, 2265–2280, https://doi.org/10.1175/JTECH-D-15-0039.1.

Lien, G.-Y., T. Miyoshi, and E. Kalnay, 2016: Assimilation of TRMM multisatellite precipitation analysis with a low-resolution NCEP global forecast system. *Mon. Wea. Rev.*, **144**, 643–661, https://doi.org/10.1175/MWR-D-15-0149.1.

Liu, C., R. P. Allan, M. Brooks, and S. Milton, 2014: Comparing tropical precipitation simulated by the Met Office NWP and climate models with satellite observations. *J. Appl. Meteor. Climatol.*, **53**, 200–214, https://doi.org/10.1175/JAMC-D-13-082.1.

Liu, G., and Y. Fu, 2001: The characteristics of tropical precipitation profiles as inferred from satellite radar measurements. *J. Meteor. Soc. Japan*, **79**, 131–143, https://doi.org/10.2151/jmsj.79.131.

Maggioni, V., P. C. Meyers, and M. D. Robinson, 2016: A review of merged high-resolution satellite precipitation product accuracy during the Tropical Rainfall Measuring Mission (TRMM) era. *J. Hydrometeor.*, **17**, 1101–1117, https://doi.org/10.1175/JHM-D-15-0190.1.

McCollum, J. R., and R. R. Ferraro, 2003: Next generation of NOAA/NESDIS TMI, SSM/I, and AMSR-E microwave land rainfall algorithms. *J. Geophys. Res.*, **108**, 8382, https://doi.org/10.1029/2001JD001512.

——, and ——, 2005: Microwave rainfall estimation over coasts. *J. Atmos. Oceanic Technol.*, **22**, 497–512, https://doi.org/10.1175/JTECH1732.1.

Mega, T., and S. Shige, 2016: Improvements of rain/no-rain classification methods for microwave radiometer over coasts by dynamic surface-type classification. *J. Atmos. Oceanic Technol.*, **33**, 1257–1270, https://doi.org/10.1175/JTECH-D-15-0127.1.

Nesbitt, S. W., and E. J. Zipser, 2003: The diurnal cycle of rainfall and convective intensity according to three years of TRMM measurements. *J. Climate*, **16**, 1456–1475, https://doi.org/10.1175/1520-0442-16.10.1456.

Ogino, S.-Y., M. D. Yamanaka, S. Mori, and J. Matsumoto, 2016: How much is the precipitation amount over the tropical coastal region? *J. Climate*, **29**, 1231–1236, https://doi.org/10.1175/JCLI-D-15-0484.1.

Petersen, W., and S. Rutledge, 2001: Regional variability in tropical convection: Observations from TRMM. *J. Climate*, **14**, 3566–3586, https://doi.org/10.1175/1520-0442(2001)014<3566:RVITCO>2.0.CO;2.

Prigent, C., F. Aires, and W. Rossow, 2006: Land surface microwave emissivities over the globe for a decade. *Bull. Amer. Meteor. Soc.*, **87**, 1573–1584, https://doi.org/10.1175/BAMS-87-11-1573.

Pu, Z., W.-K. Tao, S. Braun, J. Simpson, Y. Jia, J. Halverson, W. Olson, and A. Hou, 2002: The impact of TRMM data on mesoscale numerical simulation of Supertyphoon Paka. *Mon. Wea. Rev.*, **130**, 2448–2458, https://doi.org/10.1175/1520-0493(2002)130<2448:TIOTDO>2.0.CO;2.

Seto, S., N. Takahashi, and T. Iguchi, 2005: Rain/no-rain classification methods for microwave radiometer observations over land using statistical information for brightness temperatures under no-rain conditions. *J. Appl. Meteor.*, **44**, 1243–1259, https://doi.org/10.1175/JAM2263.1.

——, T. Kubota, N. Takahashi, T. Iguchi, and T. Oki, 2008: Advanced rain/no-rain classification methods for microwave radiometer observations over land. *J. Appl. Meteor. Climatol.*, **47**, 3016–3029, https://doi.org/10.1175/2008JAMC1895.1.

——, ——, T. Iguchi, N. Takahashi, and T. Oki, 2009: An evaluation of over-land rain rate estimates by the GSMaP and GPROF algorithms: The role of lower-frequency channels. *J. Meteor. Soc. Japan*, **87A**, 183–202, https://doi.org/10.2151/jmsj.87A.183.

Shige, S., and C. Kummerow, 2016: Precipitation-top heights of heavy orographic rainfall in the Asian monsoon region. *J. Atmos. Sci.*, **73**, 3009–3024, https://doi.org/10.1175/JAS-D-15-0271.1.

——, S. Kida, H. Ashiwake, T. Kubota, and K. Aonashi, 2013: Improvement of TMI rain retrievals in mountainous areas. *J. Appl. Meteor. Climatol.*, **52**, 242–254, https://doi.org/10.1175/JAMC-D-12-074.1.

——, M. K. Yamamoto, and A. Taniguchi, 2014: Improvement of TMI rain retrieval over the Indian subcontinent. *Remote Sensing of the Terrestrial Water Cycle*, *Geophys. Monogr.*, Vol. 206, Amer. Geophys. Union, 27–42.

Simpson, J., R. F. Adler, and G. R. North, 1988: A proposed Tropical Rainfall Measuring Mission (TRMM) satellite. *Bull. Amer. Meteor. Soc.*, **69**, 278–295, https://doi.org/10.1175/1520-0477(1988)069<0278:APTRMM>2.0.CO;2.

Sohn, B., G.-H. Ryu, H.-J. Song, and M.-L. Ou, 2013: Characteristic features of warm-type rain producing heavy rainfall over the Korean Peninsula inferred from TRMM measurements.

Mon. Wea. Rev., **141**, 3873–3888, https://doi.org/10.1175/MWR-D-13-00075.1.

Spencer, R. W., H. M. Goodman, and R. E. Hood, 1989: Precipitation retrieval over land and ocean with the SSM/I: Identification and characteristics of the scattering signal. *J. Atmos. Oceanic Technol.*, **6**, 254–273, https://doi.org/10.1175/1520-0426(1989)006<0254:PROLAO>2.0.CO;2.

Takayabu, Y. N., 2002: Spectral representation of rain profiles and diurnal variations observed with TRMM PR over the equatorial area. *Geophys. Res. Lett.*, **29**, 1584, https://doi.org/10.1029/2001GL014113.

——, S. Shige, W.-K. Tao, and N. Hirota, 2010: Shallow and deep latent heating modes over tropical oceans observed with TRMM PR spectral latent heating data. *J. Climate*, **23**, 2030–2046, https://doi.org/10.1175/2009JCLI3110.1.

Tan, J., W. A. Petersen, and A. Tokay, 2016: A novel approach to identify sources of errors in IMERG for GPM ground validation. *J. Hydrometeor.*, **17**, 2477–2491, https://doi.org/10.1175/JHM-D-16-0079.1.

Taniguchi, A., and Coauthors, 2013: Improvement of high-resolution satellite rainfall product for typhoon Morakot (2009) over Taiwan. *J. Hydrometeor.*, **14**, 1859–1871, https://doi.org/10.1175/JHM-D-13-047.1.

Tao, W.-K., S. Lang, J. Simpson, and R. Adler, 1993: Retrieval algorithms for estimating the vertical profiles of latent heat release: Their applications for TRMM. *J. Meteor. Soc. Japan*, **71**, 685–700, https://doi.org/10.2151/jmsj1965.71.6_685.

Tian, Y., and Coauthors, 2009: Component analysis of errors in satellite-based precipitation estimates. *J. Geophys. Res.*, **114**, D24101, https://doi.org/10.1029/2009JD011949.

——, C. D. Peters-Lidard, R. F. Adler, T. Kubota, and T. Ushio, 2010: Evaluation of GSMaP precipitation estimates over the contiguous United States. *J. Hydrometeor.*, **11**, 566–574, https://doi.org/10.1175/2009JHM1190.1.

Wang, N.-Y., C. Liu, R. Ferraro, D. Wolff, E. Zipser, and C. Kummerow, 2009: TRMM 2A12 land precipitation product-status and future plans. *J. Meteor. Soc. Japan*, **87A**, 237–253, https://doi.org/10.2151/jmsj.87A.237.

Wang, Y., Y. You, and M. Kulie, 2018: Global virga precipitation distribution derived from three spaceborne radars and its contribution to the false radiometer precipitation detection. *Geophys. Res. Lett.*, **45**, 4446–4455, https://doi.org/10.1029/2018GL077891.

Weng, F., B. Yan, and N. C. Grody, 2001: A microwave land emissivity model. *J. Geophys. Res.*, **106**, 20 115–20 123, https://doi.org/10.1029/2001JD900019.

Wilks, D. S., 2011: *Statistical Methods in the Atmospheric Sciences*. International Geophysics Series, Vol. 100, Academic Press, 704 pp.

Yamamoto, M. K., and S. Shige, 2015: Implementation of an orographic/nonorographic rainfall classification scheme in the GSMaP algorithm for microwave radiometers. *Atmos. Res.*, **163**, 36–47, https://doi.org/10.1016/j.atmosres.2014.07.024.

——, I. Tanaka, and S. Shige, 2017: Improvement of the rain/no-rain classification method for microwave radiometers over the Tibetan Plateau. *IEEE Geosci. Remote Sens. Lett.*, **14**, 626–630, https://doi.org/10.1109/LGRS.2017.2666814.

Yong, B., D. Liu, J. J. Gourley, Y. Tian, G. J. Huffman, L. Ren, and Y. Hong, 2015: Global view of real-time TRMM multisatellite precipitation analysis: Implications for its successor global precipitation measurement mission. *Bull. Amer. Meteor. Soc.*, **96**, 283–296, https://doi.org/10.1175/BAMS-D-14-00017.1.

You, Y., and G. Liu, 2012: The relationship between surface rainrate and water paths and its implications to satellite rainrate retrieval. *J. Geophys. Res.*, **117**, D13207, https://doi.org/10.1029/2012JD017662.

——, F. J. Turk, Z. S. Haddad, L. Li, and G. Liu, 2014: Principal components of multifrequency microwave land surface emissivities. Part II: Effects of previous-time precipitation. *J. Hydrometeor.*, **15**, 20–37, https://doi.org/10.1175/JHM-D-13-07.1.

Zipser, E. J., C. Liu, D. J. Cecil, S. W. Nesbitt, and D. P. Yorty, 2006: Where are the most intense thunderstorms on Earth? *Bull. Amer. Meteor. Soc.*, **87**, 1057–1072, https://doi.org/10.1175/BAMS-87-8-1057.